Flexible photonic-crystal Fano filters based on transferred semiconductor nanomembranes

Weidong Zhou[1], Zhenqiang Ma[2], Hongjun Yang[1], Zexuan Qiang[1], Guoxuan Qin[2], Huiqing Pang[2], Li Chen[1], Weiquan Yang[1], Santhad Chuwongin[1] and Deyin Zhao[1]

[1] Department of Electrical Engineering, NanoFAB Center, University of Texas at Arlington, TX 76019, USA

[2] Department of Electrical and Computer Engineering, University of Wisconsin-Madison, WI 53706, USA

E-mail: wzhou@uta.edu and mazq@engr.wisc.edu

Abstract

Crystalline semiconductor nanomembranes (NMs), which are transferable, stackable, bondable and manufacturable, offer unprecedented opportunities for unique and novel device applications. We report and review here nanophotonic devices based on stacked semiconductor NMs that were built on Si, glass and flexible PET substrates. Photonic-crystal Fano resonance based surface-normal optical filters and broadband reflectors have been demonstrated with unique angle and polarization properties. Such a low temperature NM stacking process can lead to a paradigm shift on silicon photonic integration and inorganic flexible photonics.

(Some figures in this article are in colour only in the electronic version)

1. Introduction

Crystalline semiconductor nanomembranes (NMs), which are transferable, stackable, bondable and manufacturable, offer unprecedented opportunities for unique electronic and photonic devices for vertically stacked high density photonic/electronic integration, high performance flexible electronics and flexible photonics. High quality single crystalline silicon NMs (Si NM) have been transferred onto various foreign substrates, such as glass and flexible polyethylene terephthalate (PET) plastics, based on low temperature transfer and stacking processes, developed by various groups [1–7]. In the last few years, significant progress has been made by Ma's group on record high-speed flexible electronics, and high performance flexible Ge photodetectors, based on transferable Si/SiGe NMs [4, 5, 8]. Many excellent results have also been reported by Lagally *et al* [6, 9, 10] and Rogers *et al* [11–14] on the unique electronic, photonic and thermoelectronic and mechanical properties associated with this new class of inorganic flexible semiconductor membrane material system.

Recently, employing a slightly modified transfer process, we have jointly demonstrated Fano filters based on patterned Si NMs transferred onto transparent low index glass and flexible PET substrates [15–19]. In this paper, we review and report the design, fabrication and characterization of these unique photonic devices, with focus on the spectral, angular, and polarization properties, based on dispersion engineering [16].

2. Fano resonant filter design

Photonic-crystal slabs (PCSs) are one of the most promising artificial platforms with in-plane periodic modulation of dielectric constant on a wavelength scale. Shown in figure 1(*a*) is the schematic of a square lattice PCS, where key lattice parameters are denoted as r, a and t, for air hole radius, lattice constant and slab thickness, respectively. The out-of-the-plane optical mode coupling is feasible with the Fano or guided resonance effect [20–23], where these in-plane guided resonances above the lightline are also strongly coupled to out-of-the-plane radiation modes due to phase matching provided by the periodic lattice structure. Therefore, the
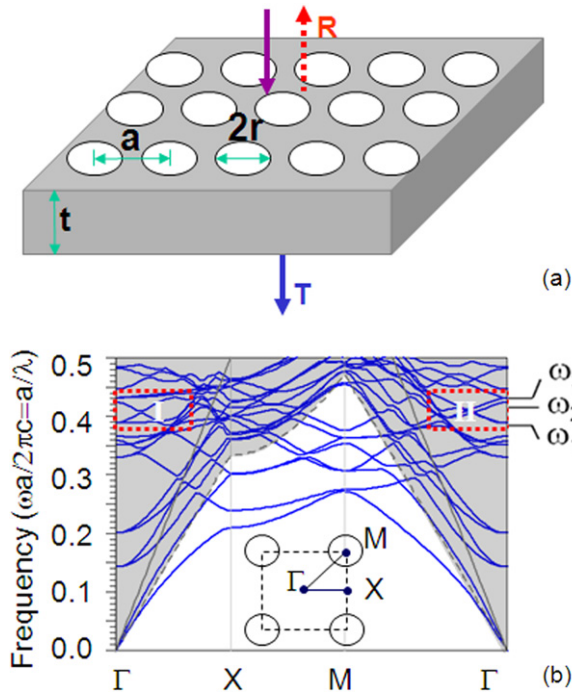
Figure 1. (*a*) Schematic of PCS with square lattice air hole patterns for surface-normal Fano filters and (*b*) Simulated dispersion characteristics for the square lattice Si PCS structure transferred onto glass/PET substrates with substrate index of 1.5. (Colour online.)

guided resonances can provide an efficient way to channel light from within the slab to the external environment, and vice versa [24]. In recent years, devices based on Fano resonance such as narrowband filters [22, 25, 26] or broadband reflectors [27, 28] have been reported. Shown in figure 1(*b*) is the simulated dispersion plot for the square lattice PCS structure shown in figure 1(*a*), based on a three-dimensional (3D) plane wave expansion (PWE) technique. The Fano resonance modes operating above the lightline region, denoted as the shaded area, are shown in figure 1(*b*). The properties of a few Fano resonance modes (ω_1, ω_2, ω_3) will be discussed later in this paper.

Photonic-crystal (PC) structures were first designed with a three-dimensional finite-difference time domain (3D FDTD) technique by using a periodic boundary condition (PBC) and a perfectly matched layer (PML) in the four lateral and two vertical directions, respectively [16], as shown in figure 2(*a*). A Gaussian source is launched from the top of the PCS structure, with two power monitors monitoring the power both reflected and transmitted. Depending on the PCS lattice parameters, either Fano resonance filters or broadband reflectors can be realized with different Q values. A set of simulated spectra for transmission and for reflection spectra is shown in figure 2(*b*) and figure 2(*c*), respectively. High Q filters with Q greater than 1000 can be easily obtained when a smaller r/a value is used ($r/a = 0.08$ for high Q case here). On the other hand, a larger r/a value can lead to lower Q filters for broadband reflector design ($r/a = 0.28$ for low Q case here).

The resonance modes were further verified with the field propagation plots based on 3D FDTD simulations. Snapshots

of field propagation for the on- and the off-resonance modes are shown in figures 3(*a*) and (*b*), respectively. Note that, for the on-resonance mode (λ_1), the surface-normal incident light is bounced back from the patterned SiNM structure due to the coherence (in-phase) reflection, which leads to the dip in the transmission spectra. On the other hand, light at other spectra locations (off-resonance) can pass through the patterned SiNM Fano filter with its maximum transmission efficiency.

3. Crystalline semiconductor NM transfer

Heterogeneous integration is currently the most promising approach to high performance photonic devices (also applicable to high-speed electronics), considering the tremendous difficulty in engineering indirect bandgap materials (e.g. Si and Ge). This argument is evidenced by the recent successes on the hybrid Si evanescent laser, the photonic devices based on the InP-bonding-to-Si structure [29, 30], and the InAs/Si heterogeneous electronics made by Intel and IBM. Over the last few years, Ma's and Rogers' groups have developed different types of NM transfer and stacking processes on Si, Ge, GaAs, InP, etc. Very high performance electronics based on transferable Si/SiGe NMs have already been reported [2–5]. Figure 4 shows a general process flow for crystalline NM release, transfer and stacking. The source material (e.g. silicon-on-insulator (SOI), GeOI, III–V multi layers with a sacrificial layer) is first being patterned into membrane (or strip forms) down to the sacrificial layer (figures 4(*a*)–(*b*)). Top membrane layers are then released by undercutting the sacrificial layer (figure 4(*c*)), and the fully released membrane settles down on the handling substrate via van der Waals force (figure 4(*d*)) (note that this in-place bonding case only applies to thin sacrificial layers. For thick ones, please refer to another paper from Rogers' group [31]. Finally NM transfer process can take place with either a *Direct flip transfer or stamp-assisted transfer* processes (figures 4(*e*)–(*f*)). In the *direct flip transfer* process, an adhesion layer is applied on the host (foreign) substrate first. The NM to be transferred can be picked up by the host substrate directly to complete the transfer. The adhesion layer (e.g. glue) can be dissolved afterwards, if needed. In the *stamp-assisted transfer* process, a stamp (e.g. PDMS) was used to press towards the handling substrate, and lift up the NM to be transferred. Then the NM attached to the stamp was picked up and attached to a new host substrate, which can be coated with glue, if needed. Slowly peeling off the stamp or removing the stamp with shear force, the NM can be left on the new host substrate [32].

Based on a slightly modified NM transfer process, high quality PCS structures have been successfully transferred onto glass or PET substrates, as shown in figure 5. PCS structures were first fabricated with the target Fano filter wavelength of 1550 nm on 260 nm thick SOI wafers using e-beam lithography and plasma dry-etching processes. Shown in figure 5(*a*) are a schematic (top) and scanning electron micrographs (SEMs, bottom) of the patterned PC SOI structures, respectively. The periodicity and air hole radius in this structure are 600 nm and 108 nm, respectively [15, 16]. The patterned PC SOI structures were subsequently immersed in aqueous diluted
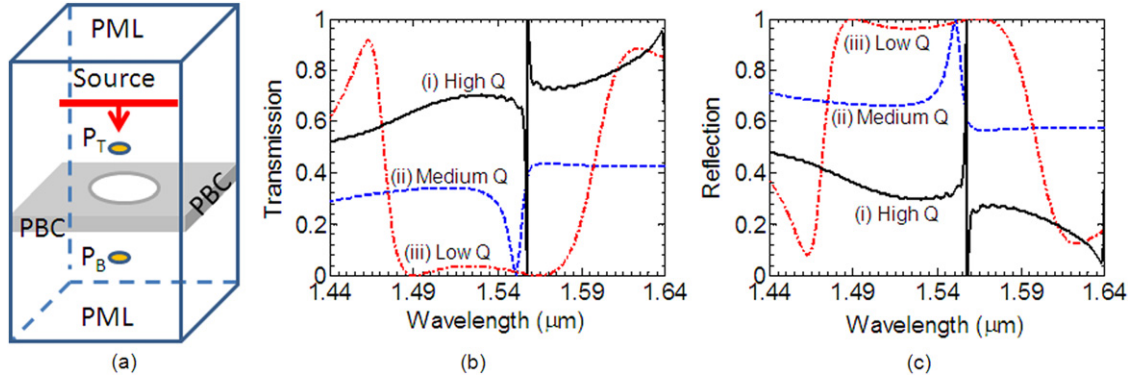
Figure 2. (*a*) Schematic of a unit cell used in the simulation based on the 3D FDTD technique; Simulated (*b*) transmission and (*c*) reflection spectra for surface-normal Fano filters with different quality factors (*Q*s) for either highly spectrally selective filters or broadband reflectors. (Colour online.)
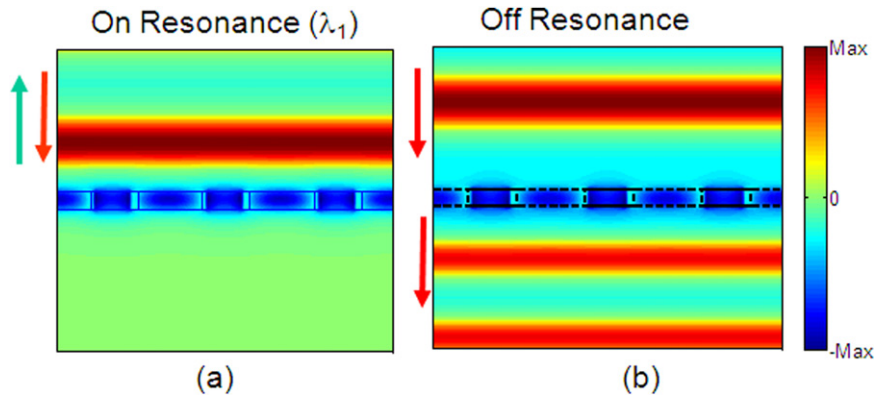

Figure 3. Snapshots of electric field distribution of Fano filters under (*a*) on-resonance and (*b*) off-resonance conditions. (Colour online.)

HF solution (49% HF : DIwater = 1 : 4) for several hours to etch away the BOX (buried oxide) layer selectively (figure 5(*b*)). Once the top patterned PC SiNM was completely released, it was rinsed in DI water and transferred onto PET flexible plastic or glass substrates (figure 5(*c*)). A micrograph is shown in figure 5(*c*, iv), where a large piece of NM was transferred onto a flexible (curved) PET substrate. The high quality large-area uniform pattern was also verified with the well-defined diffraction pattern [16]. Another set of samples was used for the polarization-dependent study (section 6) with slight variations in the lattice parameters, where the air hole radius is 118 nm and the slab thickness is 250 nm.

4. Surface-normal transmission properties

Figure 6 shows the schematic of our transmission measurement setup where an unpolarized broadband QTH (quartz tungsten halogen) lamp source was focused into a small beam size with a polarizer and an objective lens. By precisely controlling the sample holder, we can perform the transmission tests at different light incident angles defined by two specified polar angles, the colatitude angle θ (angle from the surface normal direction) and the azimuth angle ϕ as defined in figure 7. Additionally, we can also control the incident beam polarization (*E*-vector) Ψ, which is defined as the angle between the polarization direction and the PC lattice

ΓX direction. Also shown in figure 7 are the conventional definition of wave vector directions and the corresponding Brillouin zone in *k*-space with high symmetric points defined with Γ, *X* and *M*, respectively.

The measured Fano filter transmission characteristics are shown in figure 8(*a*). The experiment was conducted with an unpolarized and focused broadband QTH (quartz tungsten halogen) lamp source. The focused beam size is $\sim$150 μm in diameter, much smaller than the 1–5 mm patterned device area, but sufficiently larger than the lattice constant *a* of 600 nm. The measured transmission spectra of SiNM were obtained by normalizing the measured transmission spectral intensity data for Fano filters to the data obtained for the glass or PET substrates (reference). At certain spectral locations, close to 100% transmission was obtained. A dominant dip was observed at the target wavelength of 1547 nm (denoted as λ_1) and two other dips were observed at around 1417 nm (λ_2) and 1393 nm (λ_3), respectively.

Rigorous coupled-wave analysis (RCWA) [33, 34] was also carried out to find out the target resonance wavelength at 1547 nm for the square lattice silicon PCS on the glass substrate. The dotted blue curve shown in figure 8(*a*) is the simulated transmission response of such a structure under surface-normal conditions, which agrees very well with the measured transmission spectra. The spectral bandwidth and quality factor of the filter resonance can be further optimized to have either very high *Q* (>1000), or very low *Q* (broadband),
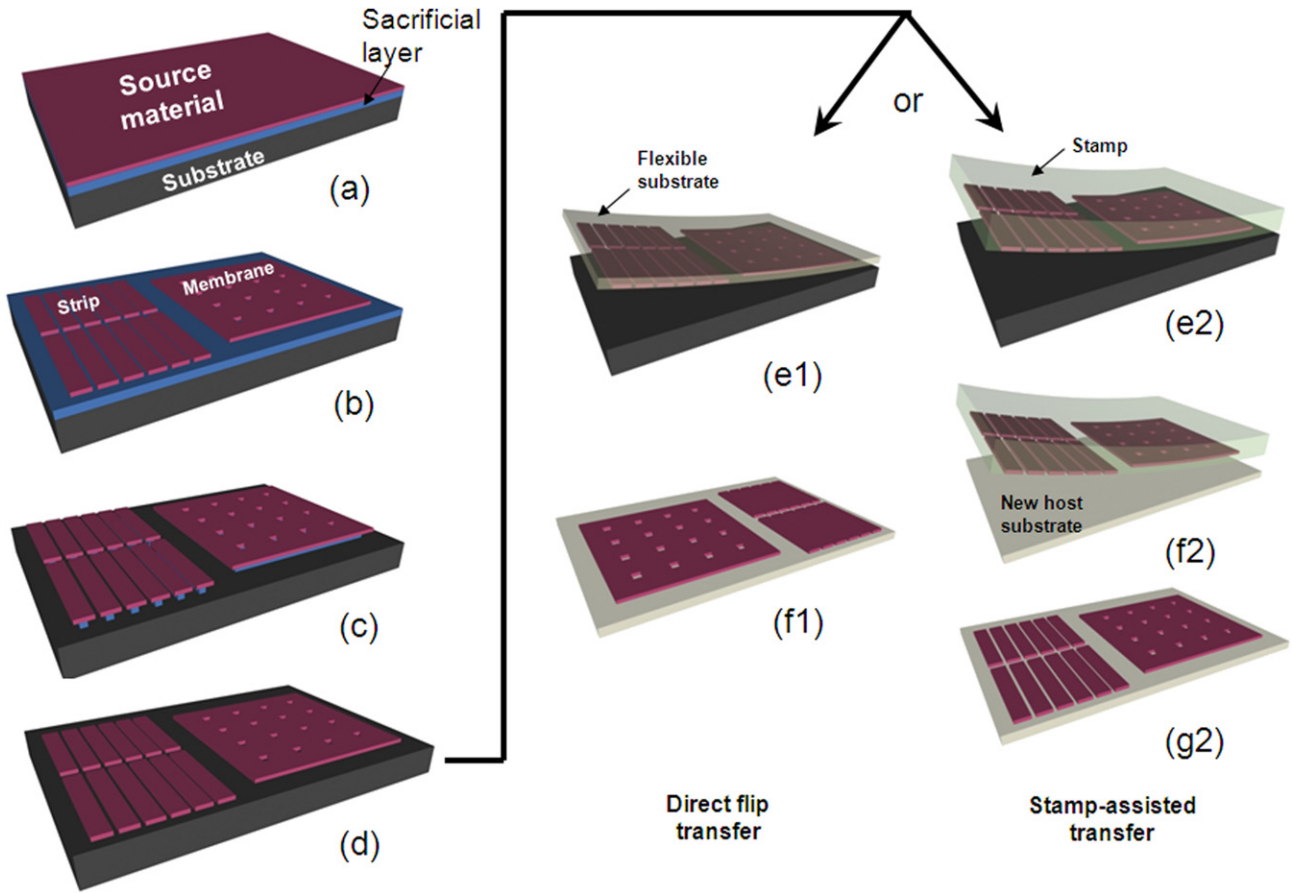
Figure 4. General process illustration for crystalline semiconductor membrane release, transfer and stacking. (*a*) Begin with source material (e.g. SOI, GeOI, III–V multi layers with a sacrificial layer). Metallization can be applied here, if needed. (*b*) Pattern top layer into membrane (or strip forms) down to the sacrificial layer. (*c*) Release membrane by undercutting the sacrificial layer. (*d*) Fully released membrane settles down on the handling substrate via van der Waals force ('in-place bonding'). *Direct flip transfer:* (e1). Apply glue on host (e.g. flexible) substrate and attach it to the handling substrate. (f1) Lift-up the host substrate and flip to complete the transfer. Glue can be dissolved if needed. *Stamp-assisted transfer:* (e2) bring a stamp (e.g. polydimethylsiloxane, or PDMS) towards the handling substrate, press and lift up. (f2) Apply the stamp with membrane attached to a new host substrate (which can be coated with glue, but not necessary). (g2) Slowly peel off the stamp or remove the stamp with shear force, leaving the membrane to stay on the new host substrate. Multiple layers can be applied by repeating (*a*)–(f1) or (*a*)–(g2). (Colour online.)
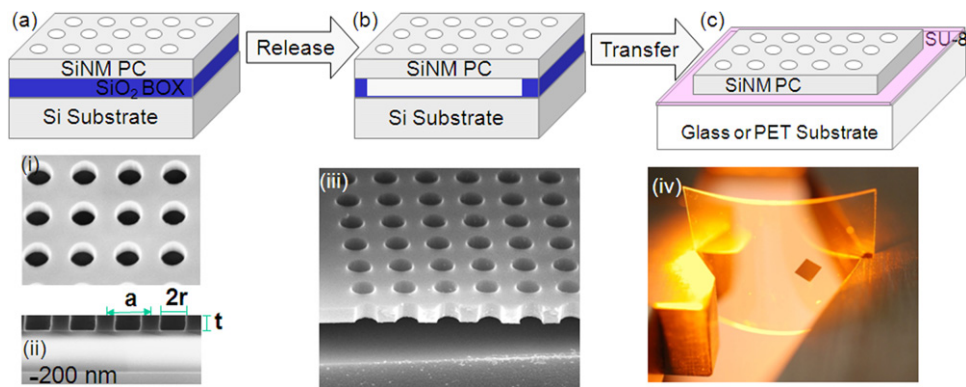

Figure 5. Modified process for air hole PCS NM structure transfer. Single layer NM pattern (*a*), release (*b*) and transfer (*c*) process, along with experimental results (bottom): (i) SEM image of top and (ii) cross-sectional view of patterned Si NM on SOI, (iii) SEM images of patterned SiNM after BHF etching of BOX layer underneath the pattern area, (iv) a micrograph of a 3 × 3 mm patterned NM transferred onto 1 inch × 1 inch flexible PET substrate. (Colour online.)

by design optimization, control of modal symmetry, choice of lattice configurations and choice of lattice parameters. The choice in the fill factor, i.e. r/a ratio, can significantly alter the device characteristics. As shown in figure 2, typically, smaller

fill factors can lead to high Q narrow band filters, and larger fill factors can lead to broadband filters/reflectors [22].

It is worth mentioning that the measured transmission spectra agree very well with the original design, with a slight
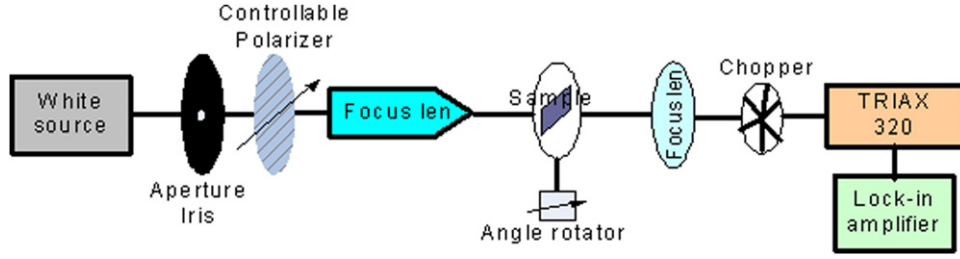
Figure 6. Schematic of transmission measurement setup using white light source and objective lens. (Colour online.)
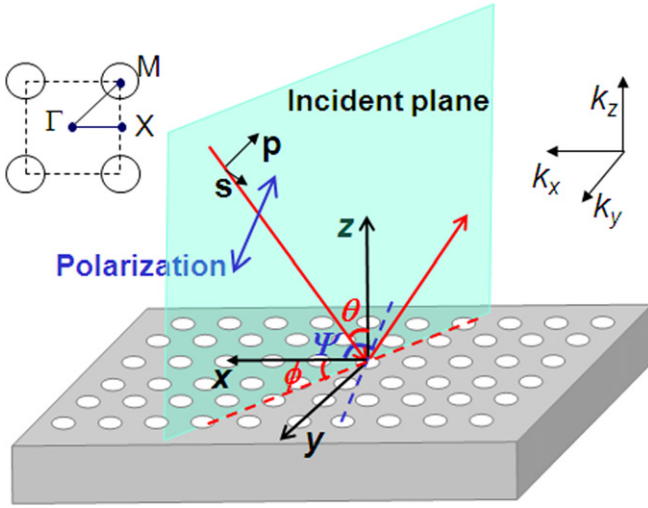

Figure 7. Angle and polarization definitions for incident light beam onto patterned SiNM Fano filters. The PC lattice and Brillouin zone symmetric points (Γ, X and M) in the k-space are also shown in the inset. (Reprinted from [17], copyright 2009, with permission from the Optical Society of America.) (Colour online.)

shift in the resonance locations. Care was taken to ensure that the fabricated device has the same lattice parameters (air hole radius r and lattice constant a). In order to fit the measured resonance locations, SiNM thickness was adjusted from the design value of 260 nm to the fit value of 250 nm, within the thickness variation specifications from the SOI wafer datasheet (Soitec®). Excellent agreement was obtained between simulations and experiment.

Note that strong oscillations in the simulated transmission spectra are due to the Fabry–Perot interferences caused by the truncated finite thickness of glass substrate during simulation. By comparing simulation and experiment, one can see that the differences in the quality factor and thus the Bloch mode lifetime [35] are small (<10%). However, the transmission contrast ratio seems to be large (4 dB difference for spectra shown in figure 2(*a*)). This could be due to our measurement uncertainty, as well as fabrication imperfections.

Additionally, these three resonance modes can be correlated with the bandedge mode at the zone centre (Γ point) for the surface-normal incident beams. All the three dips obtained in the transmission spectra (λ_1, λ_2 and λ_3) agree well with the three modes obtained from the simulated dispersion plot (figure 1(*b*)), labelled as ω_1, ω_2 and ω_3, respectively [16].

5. Angular-dependent transmission

We then analysed the angular- and polarization-dependent characteristics of Fano filters with transferred SiNM on PET substrate. Figure 8(*b*) shows the polarization dependence of our filters under surface-normal incidence by rotating the sample with different angles, ϕ, defined in figure 7. Very little spectral shifts were observed for all three aforementioned Fano resonant modes (λ_{1-3}). This is in agreement with previously reported results based on free-standing structures [36].

However, when the incident angle θ changes, all these Fano resonance modes show different kinds of shifting behaviour [16, 17]. Figure 9(*a*) shows the results of one representative case, the incident beam with $\phi = 0°$ and $\Psi = 0°$, i.e. the incident beam plane is kept parallel to the ΓX direction. Comparing with the surface-normal transmission spectra shown in figure 8(*b*), it is interesting to note that the dominant Fano resonant mode (λ_1) remains almost unchanged over the range of angles that we measured (from $0°$ to $20°$). At the same time, the other two modes (λ_2 and λ_3) shift towards longer wavelengths with the increase in incident angle.

Similar measurements were also carried out at $\phi = 45°$ and $\Psi = 45°$, another representative case, i.e. the incident beam plane is kept parallel to the ΓM direction. Shown in figure 9(*b*), both the dominant Fano resonant mode (λ_1) and the other two modes (λ_2 and λ_3) shifted significantly. All these three modes merge at an incident angle of $\theta = 20°$.

In order to correlate the Fano resonant mode dispersion properties (figure 1(*b*)) with the angle-dependent transmission characteristics (figure 9), a detailed analysis was carried out based on the relations between the incident angles and the k vector values in the dispersion plot [16]. Following the conventional denotations, the irreducible Brillouin zone of the real space square lattice is an isosceles triangle (ΓXM), whose hypotenuse ΓM is parallel to the diagonal of each elementary square (figure 7). Considering an incident beam with incident angles denoted as θ and ϕ, the corresponding propagation wave vector k in momentum space can be related to the projected components k_x, k_y and k_z, as $k_x = k \sin\theta \cos\phi$, $k_y = k \sin\theta \sin\phi$, $k_z = k \cos\theta$ and $k = 2\pi/\lambda$, where λ is the wavelength in vacuum.

For the incident beam with wave vector k kept within the ΓX direction in the k-space, i.e. for the case shown in figure 9(*a*) with $\phi = 0°$, the momentum vector k_x can be related to the normalized momentum $k_{\Gamma-X}$ along the ΓX direction as $k_x = k_{\Gamma-X}(\frac{2\pi}{a}) \cos\phi$. Thus the normalized frequency
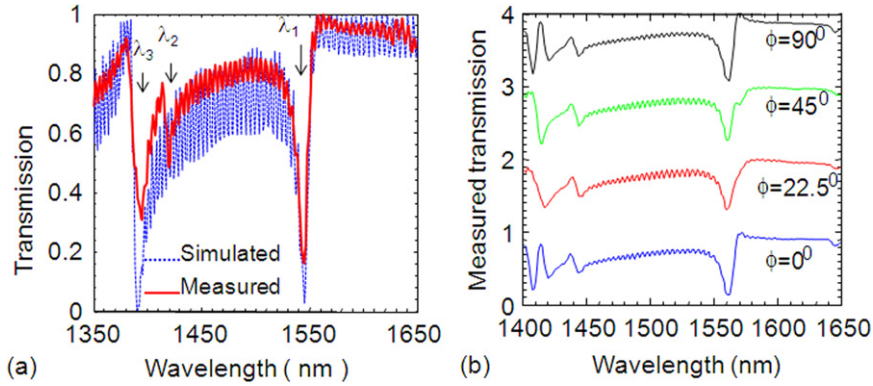
Figure 8. (*a*) Measured and simulated surface-normal transmission spectra for the fabricated patterned SiNM Fano filters on glass substrates; (*b*) measured surface-normal transmission spectra with different angles ϕ at $\Psi = 0$. (Reprinted from [17], copyright 2009, with permission from the Optical Society of America.) (Colour online.)
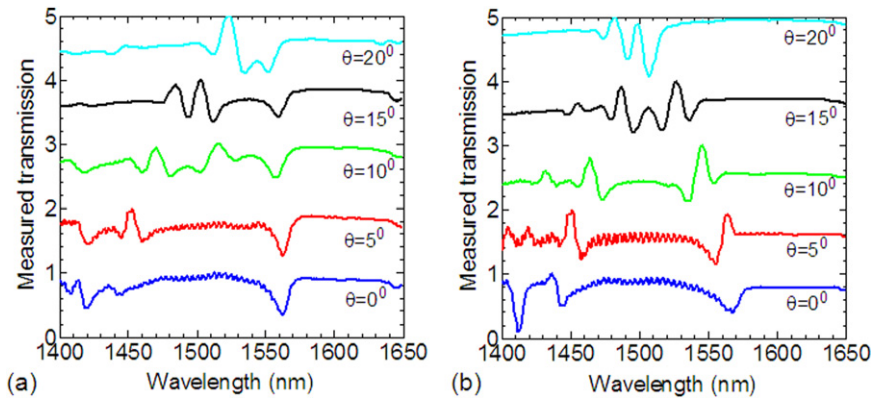

Figure 9. Measured angle-dependent transmissions with different incident angles θ or (*a*) $\phi = 0°$ and $\Psi = 0°$ and (*b*) $\phi = 45°$ and $\Psi = 45°$. (Reprinted from [16], copyright 2008, with permission from the American Institute of Physics.) (Colour online.)

(a/λ) can be related to the normalized momentum $k_{\Gamma-X}$ in the dispersion plot as $k_{\Gamma-X} = (\frac{a}{\lambda}) \sin \theta$.

A set of straight lines can be superimposed on the normalized dispersion plot, as shown in figure 10(*a*), which is the zoom-in plot of region I shown in figure 1(*b*), along the Γ–X direction. The measured Fano resonant modes were normalized and also plotted in figure 10(*a*) (circles). Excellent agreement was achieved between the experiment and the simulation results. The transmission intensity contour plots for the measured angle-dependent transmission spectra with $\phi = 0°$ (figure 9(*a*)) are also shown in figure 10(*b*), where the intensity dips/peaks are shown as the darker colours. The intensity contour plot clearly re-assembles the similar spectra shifting behaviour that is shown in figure 10(*a*).

Following a similar procedure, the measured transmission results shown in figure 9(*b*), with $\phi = 45°$, were analysed with wave vector k lying in the Γ–M plane, with results shown in figures 10(*c*) and (*d*), respectively. Again, the measurement and the simulation results agree with each other very well.

6. Polarization-dependent transmission

Polarization-dependent transmission properties were also investigated for the results shown in figures 9 and 10, in order to further understand the angle- and the polarization-dependent filter transmission characteristics [17]. As shown in

figure 7, the incident polarization (*E*-vector) angle Ψ is defined as the angle between the positive *x*-axis and the projection of the polarization direction in the *x*–*y* plane. Following a conventional definition, typical s- or p-polarizations are defined as the beam with *E*-vector perpendicular or parallel to the incident plane formed by the incident light and the reflected light, i.e. $\Psi = \phi$ for p- (TM-like) polarization and $\Psi = \phi + 90$ for s- (TE-like) polarization.

In the first case, the incident beam is restricted to be within the plane in parallel with the *x*–*z* plane, i.e. kept at $\phi = 0°$. This corresponds to the Γ–X direction in the *k*-space. The measured transmission spectra intensity contour plots for different incident angles (θ) are shown in figures 11(*a*) and (*b*) for the p- and the s-polarized incident beams, respectively. The simulated transmission spectra, based on the RCWA technique, are shown in figures 11(*c*) and (*d*), with the simulation parameters and test conditions matching the measurement results shown in figures 11(*a*) and (*b*), respectively. Note that the plots for the simulated spectra are rotated in order to have a better visual comparison between the experimental results and the simulation results.

When the incident beam is p-polarized (TM-like), i.e. the electrical vector direction lies in the plane that is in parallel with the incident beam plane, the dominant Fano resonant mode ($\lambda_1 = 1547$ nm transmission dip at $\theta = 0°$) has very little spectral shift over the range of angles measured (from 0°

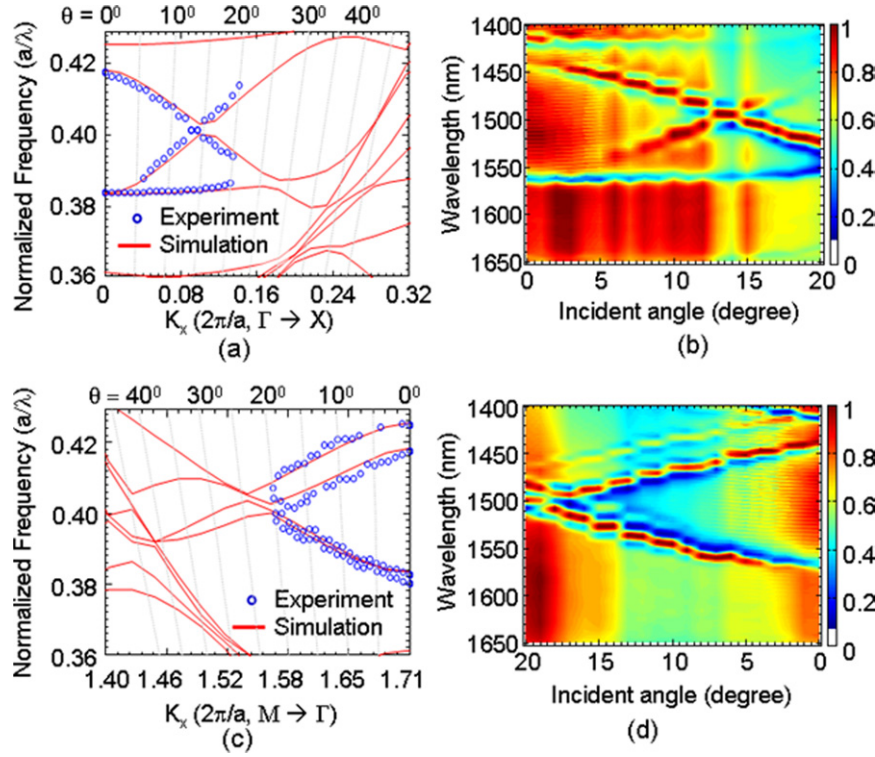**Figure 10.** (*a*), (*c*) Simulated dispersion plot (curves) zoomed in for the regions (I, II) shown in figure 2(*a*) along (Γ–X, Γ–M) directions, along with measured Fano resonances (circles) for different incident angle θ with (*a*) φ = 0° and Ψ = 0° and (*c*) φ = 45° and Ψ = 45°. The straight grey lines represent the relationships between the normalized frequency and the normalized wave-vectors along (Γ–X, Γ–M) directions. (*b*), (*d*) Measured transmission intensity contour plots for angle-dependent transmissions at different incident angle θ ith (*b*) φ = 0° and Ψ = 0° and (*d*) φ = 45° and Ψ = 45°. (Reprinted from [16], copyright 2008, with permission from the American Institute of Physics.) (Colour online.)
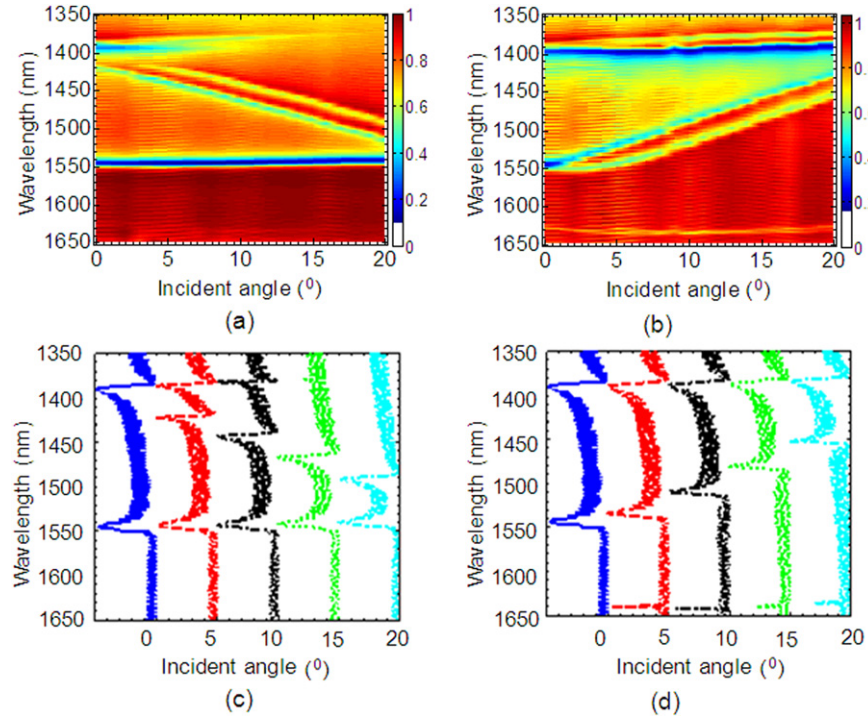

Figure 11. Measured transmission intensity contour plots under different polarization conditions (*a*) Γ–X direction with p-polarization light (*b*) Γ–X direction with s-polarization light; (*c*), (*d*) Simulated transmission spectra under p- and s-polarizations, respectively. (Reprinted from [17], copyright 2009, with permission from the Optical Society of America.) (Colour online.)
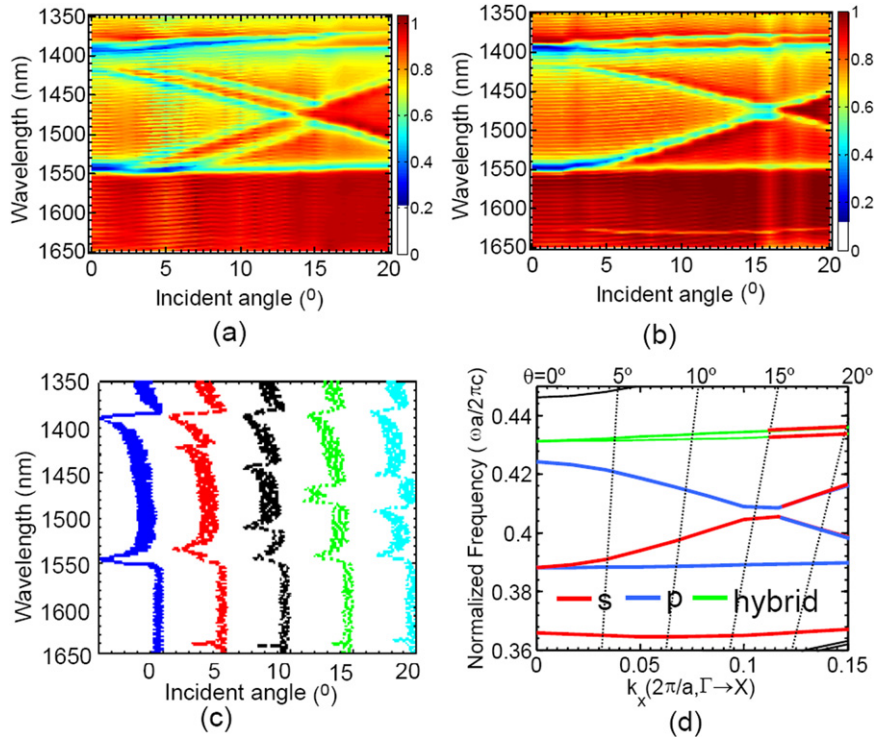
Figure 12. Measured transmission intensity contour plots for incident beam lies within *x*–*z* plane (along Γ–X direction) with (*a*) hybrid polarization ($\Psi = 45°$) and (*b*) without polarization. (*c*) Simulated transmission spectra for different incident angles with the same incident beam orientation and polarization shown in (*a*). (*d*) Dispersion plot along Γ–X shows the p- and s-polarization states. (Reprinted from [17], copyright 2009, with permission from the Optical Society of America.) (Colour online.)

to 20°). On the other hand, the other two modes show strong angle dependent behaviour. The mode at λ_2 shifted towards longer wavelengths, from 1420 nm at $\theta = 0°$ to 1500 nm at $\theta = 20°$, at a constant rate of 4 nm/°. The mode at λ_3 (1394 nm at $\theta = 0°$) shows very small angle dependence for small incident angles (from 0° to 10°). Nonetheless, it is completely suppressed for larger incident angles ($\theta > 15°$). The simulation results shown in figure 11(*c*) also agree very well with the measurement results shown in figure 11(*a*).

Different from the p-polarized beam, for an s-polarized (TE-like) incident beam, the dominant Fano resonance mode (λ_1) shifted towards shorter wavelengths (figure 11(*b*), (*d*)), from 1547 nm at $\theta = 0°$ to 1448 nm at $\theta = 20°$, at a constant rate of 5 nm/°. However, the mode at the short wavelength (λ_3) has very weak angle dependence, with a small blue-shift less than 10 nm, or 0.5 nm/°, when increasing the incident angle θ from 0° to 20°. Also note that there is no dip observed at the λ_2 location in this case.

In addition to p- and s-polarizations, incident beams with hybrid polarization ($\Psi = 45°$) were also considered. The measured transmission intensity contour is shown in figure 12(*a*). The dominant Fano resonant mode with $\lambda_1 = 1547$ nm at $\theta = 0°$ splits into two separate degenerate modes for larger incident angles, with one mode remaining at the same spectral location (p-polarization, figure 11(*a*), also confirmed later) and the other shifting towards shorter wavelengths (s-polarization, figure 11(*b*)). This result agrees very well with the data shown in figure 11 for both the p- and the s-polarized modes. In addition, with the increase in the incident angle, the

resonant mode at λ_2 shifts towards longer wavelengths and the resonant mode at λ_3 remains almost unchanged.

It is worth pointing out that such a diagonal polarization light should have both s- and p-polarization components. Therefore, in theory, it is expected that similar transmission results should be generated even from an unpolarized incident beam. This is indeed the case, as shown in figure 12(*b*), which exhibits very similar characteristics as the one shown in figure 12(*a*). The results match very well with the simulated transmission spectra based on the RCWA technique, as shown in figure 12(*c*).

Further analysis was carried out to correlate the measured transmission spectra with the Fano resonant mode based on the dispersion plot shown in figure 1(*b*). Following a similar process discussed earlier [16], a correlation was found between the incident angle θ and the wave vector k, with $k_{\Gamma-X} = (\frac{a}{\lambda})\sin\theta$. The corresponding dispersion plot is shown in figure 12(*d*), which is the zoom-in plot of region I shown in figure 1(*b*). The corresponding p-, s- and hybrid polarized modes are shown with different colours. An excellent agreement between the measurement data and the simulation results has been obtained, which also confirms the earlier analysis on the transmission spectra.

Finally, we measured the transmission characteristics for the incident beam 45° off the *x*–*z* plane, i.e. $\phi = 45°$. This is another high symmetry direction, which corresponds to the Γ–M direction in the *k*-space. Following a similar procedure, the measured transmission intensity contour for the hybrid polarization with ($\Psi = 45°$) is shown in figure 13(*a*), along with the simulated transmission spectra shown in figure 13(*b*).
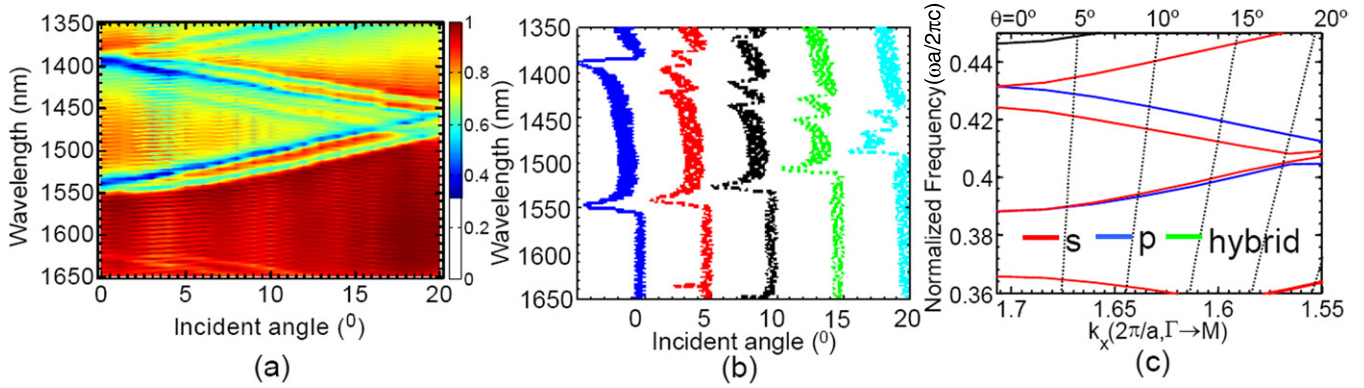
Figure 13. Measured transmission intensity contour plots for incident beam lie at 45° off x–z plane (Γ–M direction) with hybrid polarization ($\Psi = 45°$). (*b*) Simulated transmission spectra for different incident angles with the same incident beam orientation and polarization shown in (*a*). (*c*) Dispersion plot along Γ–M direction shown both p- and s-polarization states. (Reprinted from [17], copyright 2009, with permission from the Optical Society of America.) (Colour online.)
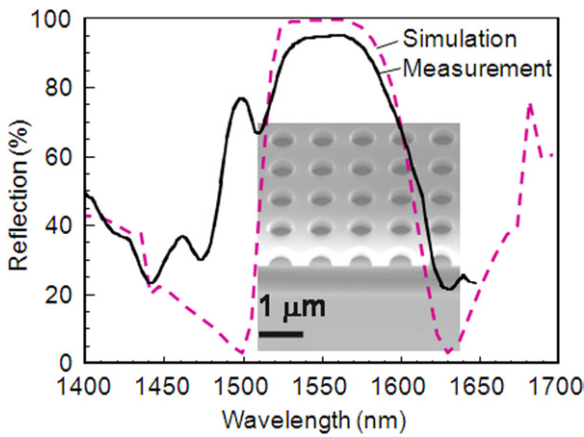

Figure 14. Measured and simulated reflection spectra for a membrane reflector with $a = 980$ nm, $r/a = 0.28$, $t_{Si} = 365$ nm and $t_{ox} = 1\,\mu$m. Shown in the inset is a cross-sectional SEM image of the fabricated Fano membrane reflector. (Modified from [19], copyright 2009, with permission from the American Institute of Physics.) (Colour online.)

The two sets of results agree very well with each other. The specific modal properties can be further explained with the dispersion plot, as shown in figure 13(*c*), for the wave vector along the Γ–M direction, which corresponds to region II shown in figure 1(*b*). Again, different polarization modes can be identified, by correlating the measured transmission spectra with the simulated dispersion curves.

7. Broadband Fano reflectors

As shown in figure 2, by properly choosing the lattice parameters, broadband reflectors can be realized. Following the similar design and fabrication process used for Fano resonant filters, we have also demonstrated broadband Fano reflectors, on Si and on glass substrates [19]. The periodicity (*a*) and air hole radius (*r*) in this square lattice structure are 980 nm and 274 nm, respectively. The thickness of the thin Si device layer is 365 nm. High quality etching is essential in achieving the desired reflection performance. Shown in figure 14 are the measured and simulated reflection spectra

for a Fano reflector fabricated on a SOI substrate, with the inset shown in the cross-sectional SEM image of the fabricated Fano reflector sample on an SOI substrate. Note that some degradation of measured maximum reflection may be due to process imperfection. Theoretically, the maximum reflection can be ∼100%. We have recently reported resonance control of the reflectors realized either by partially removing buried oxide layer underneath the device layer, or by controlled SiO_2 film deposition on top of the devices [19]. Both blue- and red-shifts were demonstrated with a turning range of 50 nm for a centre wavelength of 1550 nm. These results demonstrate practical post-process means for Fano resonance engineering for both narrow band filters and ultra-compact broadband reflectors.

8. Flexible Fano filter bending properties

We have also investigated the bending properties of these flexible Fano filters based on Si NMs on flexible PET substrates. Measured transmission spectra under different bending conditions are shown in figure 15(*a*), with the measured transmission intensity contour shown in figure 15(*b*). The major transmission features are similar to those of the unbent flat sample shown earlier. A spectral-blue shift was seen at different bending conditions, with about a 2 nm shift for a small bending case (with bending radius R of 601 mm) and a 4 nm shift for a large bending case (with R of 301 mm). The spectral shift is most likely related to the strain-induced refractive index change in Si, as well as the deformation of lattice parameters. Further work is ongoing to understand the mechanical properties of these flexible Fano filters. This is one of the first experimental results reported on flexible optical filters based on inorganic semiconductor thin films on flexible substrates.

9. Conclusions

We reviewed and reported here a new type of flexible filters based on Fano resonances in inorganic semiconductor NMs transferred onto glass or flexible PET substrates. The principles of Fano resonance and the filter design were
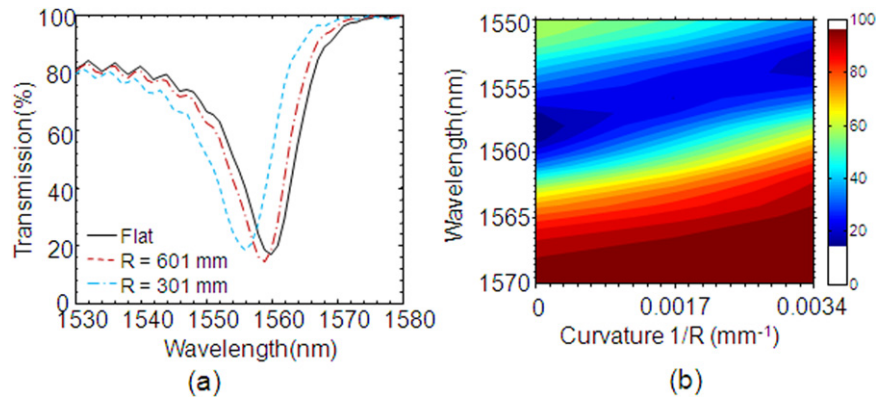
Figure 15. Flexible Fano filter bending properties: (*a*) Measured transmission spectra and (*b*) measured transmission spectra intensity contour plot for flexible filters under different bending conditions. (Colour online.)

first discussed, followed by the introduction of the wet transfer process for the realization of inorganic SiNM based flexible electronic and photonic devices. The angular-, polarization- and bending-dependent transmission properties of the filters were systematically investigated. Excellent agreement was obtained between measurement results and simulation/theoretical analysis results from 3D FDTD, RCWA and PWE techniques. It is shown that both narrow band filters and broadband reflectors can all be realized based on the design and the control of lattice parameters of PCs.

Our results show that Fano resonance based silicon NM devices can be ultra compact and flexible (note that typically a lateral lattice period of $15a$ is sufficient to achieve compact, yet high performance photonic devices [37]). With further process optimizations, transferred NMs can find wider and practical applications in various electronic and photonic device and integration system applications [18, 38, 39].

Acknowledgments

References

[1] Schmidt O G and Eberl K 2001 *Nature* **410** 168
[2] Yuan H C, Roberts M M, Zhang P, Park B N, Klein L J, Savage D E, Flack F S, Ma Z, Evans P G, Eriksson M A, Celler G K and Lagally M G 2006 *Topical Meeting on Silicon Monolithic Integrated Circuits in RF Systems (SiRF)* (San Diego, CA: IEEE) pp 327–33
[3] Yuan H C and Ma Z 2006 *Appl. Phys. Lett.* **89** 212105
[4] Yuan H C, Ma Z, Roberts M M, Savage D E and Lagally M G 2006 *J. Appl. Phys.* **100** 013708
[5] Yuan H C, Celler G K and Ma Z 2007 *J. Appl. Phys.* **102** 034501
[6] Scott S A and Lagally M G 2007 *J. Phy. D: Appl. Phys.* **40** R75–R92
[7] Rogers J, Bao Z, Baldwin K, Dodabalapur A, Crone B, Raju V, Kuck V, Katz H, Amundson K and Ewing J 2001 *Proc. Natl Acad. Sci. USA* **98** 4835–40
[8] Yuan H-C, Shin J, Qin G, Sun L, Bhattacharya P, Lagally M G, Celler G K and Ma Z 2009 *Appl. Phys. Lett.* **94** 013102
[9] Zhang P, Tevaarwerk E, Park B, Savage D, Celler G, Knezevic I, Evans P, Eriksson M and Lagally M 2006 *Nature* **439** 703–6
[10] Roberts M M, Klein L J, Savage D E, Slinker K A, Friesen M, Celler G, Eriksson M A and Lagally M G 2006 *Nature Mater.* **5** 388–93
[11] Sun Y and Rogers J A 2007 *Adv. Mater.* **19** 1897–916
[12] Kim D, Ahn J, Choi W, Kim H, Kim T, Song J, Huang Y, Liu Z, Lu C and Rogers J 2008 *Science* **320** 507
[13] Kim D, Song J, Choi W, Kim H, Kim R, Liu Z, Huang Y, Hwang K, Zhang Y and Rogers J 2008 *Proc. Natl Acad. Sci. USA* **105** 18675
[14] Rogers J and Huang Y 2009 *Proc. Natl Acad. Sci. USA* **106** 10875
[15] Yang H, Qiang Z, Pang H, Ma Z and Zhou W D 2008 *Electron. Lett.* **44** 858–9
[16] Qiang Z, Yang H, Chen L, Pang H, Ma Z and Zhou W 2008 *Appl. Phys. Lett.* **93** 061106
[17] Chen L, Qiang Z, Yang H, Pang H, Ma Z and Zhou W D 2009 *Opt. Express* **17** 8396–406
[18] Saha T and Zhou W 2009 *J. Phys. D: Appl. Phys.* **42** 085115
[19] Yang H, Chuwongin S, Qiang Z, Chen L, Pang H, Ma Z and Zhou W 2009 *Appl. Phys. Lett.* **95** 023110
[20] Fano U 1941 *J. Opt. Soc. Am.* A **31** 213–22
[21] Fano U 1961 *Phys. Rev.* **124** 1866
[22] Fan S and Joannopoulos J D 2002 *Phys. Rev.* B **65** 235112
[23] Magnusson R and Wang S S 1992 *Appl. Phys. Lett.* **61** 1022
[24] Kanamori Y, Kitani T and Hane K 2007 *Appl. Phys. Lett.* **90** 031911
[25] Lin C, Lu Z, Shi S, Jin G and Prather D W 2005 *Appl. Phys. Lett.* **87** 091102
[26] Rosenberg A *et al* 2005 *Opt. Express* **13** 6564–71
[27] Suh W and Fan S 2004 *Appl. Phys. Lett.* **84** 4905
[28] Boutami S, Bakir B B, Hattori H, Letartre X, Leclercq J-L, Rojo-Romeo P, Garrigues M, Seassal C and Viktorovitch P 2006 *IEEE Photon. Technol. Lett.* **18** 835–7
[29] Park H, Fang A, Kodama S and Bowers J 2005 *Opt. Express* **13** 9460–4
[30] Bowers J E, Park H, Fang A W, Cohen O, Jones R and Paniccia M 2006 *IEEE J. Sel. Top. Quantum Electron.* **12** 1657–63
[31] Mack S, Meitl M A, Baca A J, Zhu Z T and Rogers J A 2006 *Appl. Phys. Lett.* **88** 213101

[32] Meitl M A, Zhu Z T, Kumar V, Lee K J, Feng X, Huang Y Y, Adesida I, Nuzzo R G and Rogers J A 2006 *Nature Mater.* **5** 33–8

[33] Moharam M G and Gaylord T K 1981 *J. Opt. Soc. Am.* **71** 811–8

[34] Johnson K C 1981 *Appl. Phys.* A **24** 249–60

[35] Drouard E, Hattori H, Grillet C, Kazmierczak A, Letartre X, Rojo-Romeo P and Viktorovitch P 2005 *Opt. Express* **13** 3037–48

[36] Lousse V, Suh W, Kilic O, Kim S, Solgaard O and Fan S 2004 *Opt. Express* **12** 1575–82

[37] Huang M C Y, Zhou Y and Chang-Hasnain C J 2007 *Nature Photon.* **1** 119–22

[38] Qiang Z, Zhou W D, Lu M and Brown G J 2008 *Proc. SPIE* **6901** 69010F

[39] Zhou W and Ma Z 2010 Semiconductor nanomembranes for stacked and flexible photonics (Invited) *Photonics West 2010 (San Jose, CA)*